Nano Energy 63 (2019) 103871

Contents lists available at ScienceDirect

Nano Energy

journal homepage: www.elsevier.com/locate/nanoen

Full paper

A rotational pendulum based electromagnetic/triboelectric hybrid-generator for ultra-low-frequency vibrations aiming at human motion and blue energy applications

Cheng Hou[a,1], Tao Chen[a,1], Yunfei Li[a], Manjuan Huang[a], Qiongfeng Shi[b,c,d,e], Huicong Liu[a,*], Lining Sun[a,**], Chengkuo Lee[b,c,d,e,***]

[a] School of Mechanical and Electric Engineering, Jiangsu Provincial Key Laboratory of Advanced Robotics, Soochow University, Suzhou, 215123, China
[b] Department of Electrical &computer Engineering, National University of Singapore, 4 Engineering Drive 3, Singapore, 117576, Singapore
[c] Center for Intelligent Sensors and MEMS, National University of Singapore, E6 #05-11F, 5 Engineering Drive 1, Singapore, 117608, Singapore
[d] Hybrid-Integrated Flexible (Stretchable) Electronic Systems Program, National University of Singapore, E6 #05-4, 5 Engineering Drive 1, Singapore, 117608, Singapore
[e] National University of Singapore Suzhou Research Institute (NUSRI), Suzhou Industrial Park, Suzhou, 215123, China

ARTICLE INFO

Keywords:
Rotational Electromagnetic/triboelectric hybrid generator
Ultra-low-frequency
Human motion
Ocean wave
Blue energy harvesting

ABSTRACT

There is abundance of low-frequency biomechanical and blue energy that can be harvested from our ambient environment. Utilization of these energy plays a significant role for the sustainability of the wearable devices and environmental monitoring devices. Here, we presented a rotational pendulum triboelectric-electromagnetic hybrid generator (RPHG) which is able to scavenge low-frequency (< 5 Hz) vibration energy from both arbitrary human motion and ocean waves. Four stacked disk-shaped rotor magnets are introduced into the generator for the rotational motion. The pendulum rotor can easily rotate around the bearing by gravity or inertia force with a broadband frequency excitation, and coupled with surrounding coils to operate electromagnetic generator (EMG). In the meantime, triboelectric nanogenerator (TENG) is realized by utilizing the rotor to trigger the contact-separation mode of the copper ring and surrounding fluorinated ethylene propylene (FEP) film. The hybridized generator is very sensitive to irregular human motion and ultra-low-frequency ocean waves. After the optimization of the configuration of the hybrid generator, the maximum power density of 3.25 W/m^2 and 79.9 W/m^2 are obtained at a driving frequency of 2 Hz and amplitude of 14 cm by the TENG and EMG, respectively, which can charge a capacitor of 22 μF to 7 V rapidly in 30 s. The RPHG can light up about more than hundreds of commercial lights emitting diodes (LEDs). Then, the RPHG was placed on human body and tested by running on treadmill and rope skipping. The open-circuit voltage of the EMG can be about 9 V and that of TENG can reach 150 V. Finally, the RPHG was tested on a homemade buoy in Tai Lake. When the wave frequency is about 1 Hz and the wave height is 20 cm, the open-circuit voltage of EMG can reach over 3 V and that of TENG can reach 80 V regardless of whether the RPHG is placed vertically or horizontally. Generally, the proposed device demonstrates the effectiveness towards energy harvesting from ambient environment of multidirectional and wide frequency range, i.e., human motion and blue energy, showing the great potential of being a sustainable power source for those wearable devices and monitoring devices in blue ocean.

1. Introduction

Over the past decades, with the rapid development of microelectronics, microelectromechanical systems (MEMS) and mobile internet technology, Internet of Things (IoT) has becoming one of the next generations of information technology. More and more microsensors and actuators are being widely used in various fields, such as health monitoring, environment protection, infrastructure monitoring and security. Although the power consumption of these electronic devices is small individually, the number of such units can be huge in the order of

* Corresponding author. School of Mechanical and Electric Engineering, Jiangsu Provincial Key Laboratory of Advanced Robotics, Soochow University, Suzhou, 215123, China
** Corresponding author.
*** Corresponding author.
E-mail addresses: hcliu078@suda.edu.cn (H. Liu), lnsun@hit.edu.cn (L. Sun), elelc@nus.edu.sg (C. Lee).
[1] These authors contribute equally to this work.

https://doi.org/10.1016/j.nanoen.2019.103871
Received 25 March 2019; Received in revised form 18 June 2019; Accepted 2 July 2019
Available online 05 July 2019

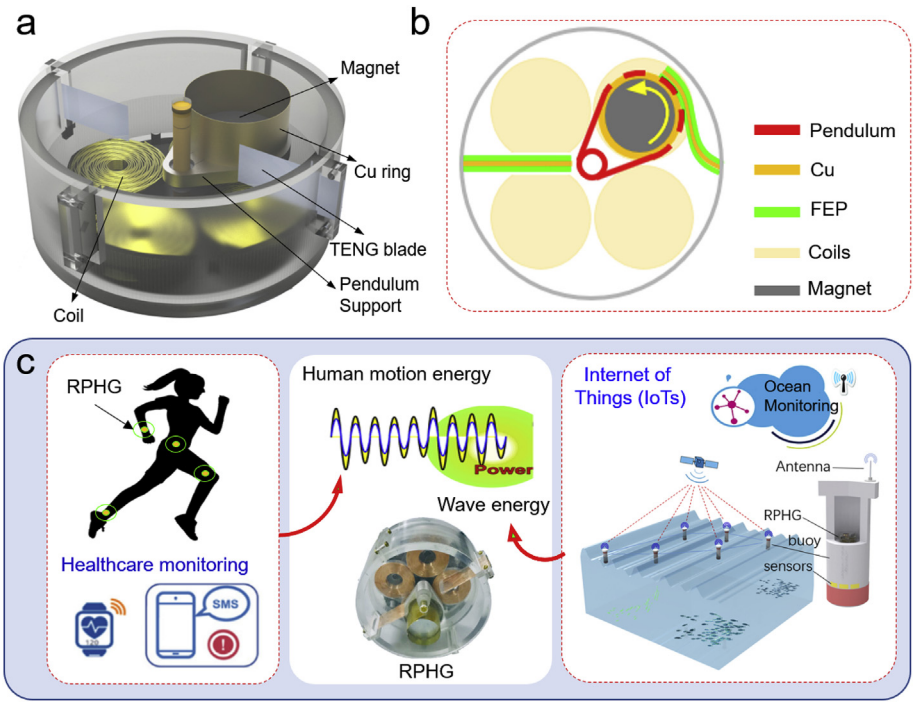

Fig. 1. Structure design of the hybrid generator. (a) Schematic illustration of the RPHG device. (b) Top view of the structure diagram of the RPHG. (c) Schematically illustration of the possible applications of the hybrid generator for human healthcare monitoring and ocean monitoring in IOT by harvesting irregular and low-frequency human motion and ocean wave energies.

billions. Traditional batteries or connecting wires do not meet the requirements of these miniature devices, such as wireless, portable, long life, environmentally friendly, and even implantable. In recent years, more and more attention has been paid to energy harvesting technique [1–9], which can convert various environmental energy into electric energy. It is considered as a reliable and independent strategy for providing continuous power source.

Human motion and blue energy have the promising prospects for producing electricity since there is a large amount of human activities on the earth and 70% surface of the earth is covered by oceans. Wave energy is one of the main sources of blue energy, which represents the energy offered by water wave, tide and ocean related. The characteristics of human motion and ocean waves are random and irregular vibrations with ultra-low frequency of less than 10 Hz, or even 1 Hz. However, the resonant frequency of these traditional resonant-based vibration energy harvesters is relatively high [10,11]. Although researchers have proposed a number of methods to reduce the resonant frequency to be less than 100 Hz or even 30 Hz, the output performance were decreased greatly [12]. This issue has inspired intensive investigations of non-resonant mechanisms to broaden the operation bandwidth and improve the energy harvesting efficiency [7,13]. But the power output of the reported energy harvesters is limited due to the ultra-low frequency and irregular magnitude and direction of vibrations. On the contrary, unlimited rotary motion of a pendulum rotor could be a good solution to eliminate the restriction of traditional harvesters [14,15].

Meanwhile, based on the coupling of triboelectrification and electrostatic induction, the triboelectric nanogenerators (TENG) [16–26] have been recognized as one of the most effective energy conversion techniques. TENG can harvest mechanical energy of broad frequency range from human motion [23,24], ocean wave [27–32], wind [33–36] and other mechanical vibrations [37], which benefit from the light weight, high output voltage, simple fabrication and good reliability. Also, TENG demonstrates high energy conversion efficiency, low cost, flexibility, and rich selection of materials [38–43]. However, one of the main disadvantages of the TENG is that the output current is very low. On the contrast, electromagnetic generator (EMG) with high output current due to the low impedance can be a complementary method. The coupling of these two energy conversion mechanisms indicates an effective approach to realize high output performance from ambient mechanical for powering miniaturized electronics [40,44].

Many works hybridized EMG and TENG together, utilizing their complementary features [45,46] with rotational structure designs, so as to capture the multidirectional and wide frequency range energies from human motion and ocean waves. Previously, Guo et al. [47] have reported a hybrid nanogenerator, which is composed of a fully encapsulated TENG and an EMG. The moving part of the TENG is indirectly driven by the magnet in the EMG, which can harvest in harsh environments. Wen et al. [48] reported a hybrid nanogenerator that consists of a spiral-interdigitated-electrode TENG and a wrap-around EMG, which could generate electricity under either rotation mode or fluctuation mode from ocean tide, current, and wave energy due to its unique structure. Although these rotating hybrid nanogenerator have high output performance, the rotation is driven by a large external force from an electric motor, water, or wind with high flow speed [49–56]. If the driven force is small, these hybrid nanogenerator could not work smoothly since the friction between the triboelectric materials.

Considering the irregular, low frequency and even multi-direction vibrations of human motion and ocean waves, we demonstrated a novel rotational pendulum design of hybridized generator (RPHG), which can be easy-driven by ultra-low-frequency and irregular motions. The RPHG consists of an EMG module and flexible TENGs module. Driven by the rotation of the pendulum rotor, the copper ring around the rotor magnets will periodically get in contact and separation with the flexible TENG blades. The optimum configuration including the number and thickness of the TENG blades have been investigated and the performance of the EMG and the TENG modules are studied. The RPHG was placed on human body and tested by running on treadmill and rope skipping, which demonstrated its effectiveness for harvesting energy from human motion. Finally, the RPHG was fixed on a homemade buoy and the output performance was verified in Tai Lake to demonstrate its effectiveness for harvesting water wave energy.

2. Results and discussion

2.1. Fabrication of the hybrid generator

The design schematic of the hybrid nanogenerator is shown in

Fig. 1a, which mainly includes a pendulum rotor, coils, TENG blades and a cylindrical frame. The pendulum rotor is composed of an aluminum alloy support, four disk-shaped magnets made of NdFeB and a copper (Cu) ring curling around the magnets, while the pendulum rotor is assembled on the center shaft by two ceramic bearings. The diameter and height of the magnets has been optimized in the following discussion. The frame is a tube structure made of acrylic with two covers on its top and bottom sides and its inner diameter and height are 65 cm and 40 cm, respectively. Four groups of coils with a circular pattern around the center shaft are embedded in the bottom cover, and each has a dimension of ∅25 mm × 4 mm. These four coils are connected in series in order to increase the output voltage. The longitudinal distance between magnets and coils is 2 mm. As shown in Fig. 1b, one piece of middle Cu electrode and FEP films on both sides form a sandwich flexible TENG blade (FEP//Cu//FEP). One side of the blade was fixed on an acrylic sheet around the frame, while the other side of the blade is freestanding. The width of the blade is 10 mm. Hereinafter, the length, thickness, number and position of the blades, were optimized. In this device, the magnets and the coils form an EMG module, while the flexible blades and Cu ring form a contact-separation TENG module. The two TENG blades are connected in parallel.

The pendulum rotor magnets can be easily driven to do clockwise and anticlockwise rotation around the center shaft by external excitation force. The motion of the rotor magnets will induce magnetic flux change across each coil and electrical voltage will be generated in the electromagnetic coil accordingly. Meanwhile, as the pendulum rotor carries the Cu ring to rotate clockwise or anticlockwise, the copper will periodically get in contact with the flexible FEP//Cu//FEP blades and scrape through it. Therefore, a contact and separation between the surfaces of the two different materials (FEP and Cu) occurs consecutively. Electricity is generated through the coupling of triboelectrification and electrostatic induction via the periodic contact and separation between two oppositely polarized triboelectric charged surfaces, resulting in the observed voltage/current signals. The installation diagram of the whole device, the pendulum rotor and the TENG blade are shown in Supporting information Fig. S1. In Fig. 1c, a proposed scheme of the RPHG for scavenging the low-frequency and irregular human motion energy is demonstrated. Also, it provides an innovative and effective approach toward large-scale blue energy harvesting. The real-time harvesting of kinetic energy can be realized through the RPHG, which is of great help to human health monitoring and intelligent Marine Internet of Things (IOT).

2.2. Working mechanism

The working mechanism of the TENG is schematically depicted in Fig. 2a. From Fig. 2a (i) to (v), the contact/separation process between the copper ring and the blade and the generation process of the electric charge and current flow can be clearly identified. At the original state, the blade remains at its neutral state without any current flow. When the Cu ring approaches the FEP film and balances the negative surface charges on FEP film, causing the electrons flow from the ground to the Cu electrode under the FEP film until they become fully contact with each other, resulting in an output signal in state ii. When the FEP film is in a fully physical contact with the Cu ring during the pendulum rotor rotation, electrons are transferred from Cu into FEP due to the higher surface electron affinity of FEP. However, no electron flow occurs in the external circuit because the produced triboelectric charges with opposite polarities are perfectly balanced. Once a relative separation occurs between the Cu ring and the FEP film, the negative charges on the surface of the FEP will induce positive charges on the Cu electrode to compensate the triboelectric charges, driving the free electrons flow from the Cu electrode to the ground as shown in state iv. This electrostatic induction process can generate an output voltage/current signal until the negative triboelectric charges on the surface of the FEP are fully screened from the transferred triboelectric charges to the Cu electrode. In state v, with the rotation of the pendulum rotor, the copper ring begins to collide with the bottom blade. Subsequently, the electrons will flow back from the ground to the electrode of the bottom blade and a reversed direction of the current can be observed. The positive triboelectric charges on the electrode of the bottom blade are gradually neutralized until the copper ring are fully contact with the bottom blade. Thereafter, they began to separate from each other. The electrons flow in the opposite direction again until the copper ring and the bottom blade are separated completely. As the rotation of the magnetic rotor continues, the copper ring starts to contact with the top blade again, resulting in the flow of electrons from Cu ring to the electrode of the top blade. Until the Cu ring and the top blade are fully contact, a full cycle of the electricity generation process completes. The Cu ring and the two TENG blades act as an electron pump to drive electrons to flow back and forth twice during one rotation cycle. Therefore, an alternating current flow can be observed in the external circuit. Likewise, an anticlockwise motion of the copper ring experiences a similar generation process of electricity with opposite current flow in the circuit. As shown in Fig. 2b, c and d, finite-element analysis (FEA) using COMSOL Multiphysics was performed to gain a more quantitative understanding of the electrical potential distribution of the TENG where the rotor drives the Cu ring to make a contact and separation with the FEP. As shown in Fig. 2b and c, the gap between the Cu ring and the FEP changes with the rotating of the rotate magnet (Fig. 2c), and the Cu ring scrapes the FEP until they are separated (Fig. 2d) resulting in a change in electrical potential distribution.

For the TENG, the open circuit voltage V_{OC} and the transfer charge Q_{SC} under short-circuit conditions can be represented as [57–59].

$$V_{OC}^{TENG} = \frac{\sigma S}{C} \tag{1}$$

$$Q_{SC}^{TENG} = \int I_{sc}\, dt \tag{2}$$

where σ is the transfer charge density, S is the contact area between the FEP and Cu electrode, and C is the capacitance.

The flexible blade can be considered as a cantilever beam, and its spring constant k is expressed as [60].

$$k = \frac{Ewt^3}{4l^3} \tag{3}$$

where E is the Young's modulus of the FEP, w is the width, t is the thickness of the FEP, and l is the length of the cantilever. The cantilever can be deformed when a concentrated load F_T of the rotational rotor magnets is applied on the FEP surface at the contacting point, as indicated in Fig. S2. The fixed end is the origin of the coordinate axis, and the deflection at the x position is

$$y(x) = \frac{2F_T x^2}{Eth^3}|x - 3a| \tag{4}$$

where x is the coordinate of any one point of the cantilever on the X-axis, a is the distance from the contacting point to the fixed point of the cantilever. Therefore, from Eq. (4), the thickness of the Cu electrode, the thickness of the FEP and the length of the blade are all important factors that affect the output performance, which will be optimized in the following experiments.

The EMG part is based on Faraday's law of electromagnetic induction. A physical model of the EMG part is illustrated in Fig. 2e. Because of the bearing support for the magnet rotor, the magnets can rotate around the shaft driven by low frequency vibration without unnecessary surface friction. Even a small acceleration of the external excitation can trigger the pendulum rotor rotate clockwise and anticlockwise around the shaft. The rotating magnet is just above the coils. Fig. 2f shows the magnetic field distribution of one magnet. The magnet flux density decreases as the distance from the object to the magnet increases. Considering the precision of machining and 3D printing, the distance between the magnet and the coil is set to 2 mm. The rotational

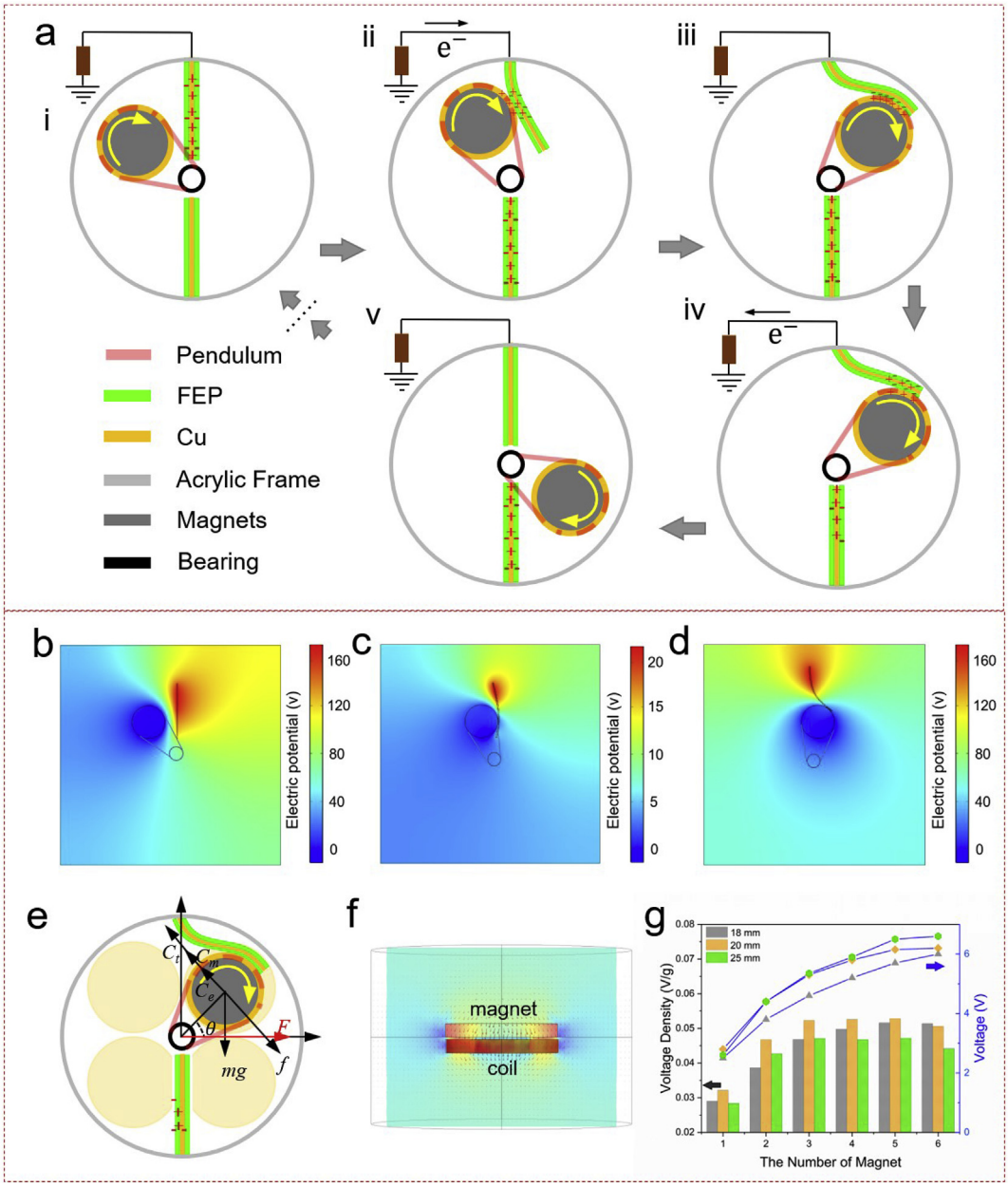

Fig. 2. Working mechanism of the hybrid generator. (a) Schematic diagram of the power generation process of the TENG with two blades in a half cycle. (b–d) electric potential distribution during contact-separation. (e) Physical model of the hybrid generator when the rotor magnets rotate. (f) Simulated magnetic field distribution of the EMG. (g) The output voltage and voltage density of the hybrid generator at a constant frequency of 2 Hz and amplitude of 8 cm with different magnets combination.

motion of the pendulum rotor magnet will induce the change of magnetic field across each coil, and the electrical voltage signals will be induced in the electromagnetic coil accordingly.

In the physical model, the RPHG is confined to be excited along x-direction and perpendicular to the ground. The pendulum rotor magnet rotates under external force F applied in the x-direction. M and m denote the mass of the housing and the rotor magnets, respectively. C_m, C_t and C_e and f denote the rotational damping force due to the friction between the bearing and shaft, rotational damping force due to the friction between the copper ring and FEP film, electric-magnetic damping force and the inertia driving force, respectively. R and θ denote the distance from the centre of rotor magnet to the centre shaft and the rotating angle of the pendulum rotor. On the basis of the dynamic characteristics of the model, the motion of the device is define as $x_m = x + (R + r)\cos\theta$ and $y_m = (R + r)\sin\theta$, where x_m and y_m denote the absolute displacements of the rotor magnet in the x- and y-directions, respectively. x denotes the reciprocating motion of the device. With the kinetic energy, potential energy, and generalized forces, the equations describing the motion of the system can be derived by using Lagrange's equations. Thus, the governing equations of the motion of the rotor magnet are written as

$$\begin{cases} (M+m)\ddot{x} + mR(\ddot{\theta}\cos\theta - \dot{\theta}^2\sin\theta) + c\dot{x} = F\cos(\omega t) \\ [mR^2 + I]\ddot{\theta} + C_m + C_e + C_t = -mR\ddot{x}\cos\theta \end{cases} \quad (5)$$

where I is the mass moment of inertia of the rotor magnet. By approximating the magnetic field of the rotor magnet to uniform, the output voltage across each coil is related to the number of turns N, the angular velocity of the rotor and the radius of the coils. The voltage can be expressed as

$$E(t) = NBLv = NB\int_{point1}^{point2} \dot{\theta} l dl \tag{6}$$

where piont1 and point2 are the coordinates of the two points at which the outer diameter of the magnet intersects the coils. When the rotor magnet rotates, there will be electric-magnetic resistance force C_e, the rotational damping force of bearing and the rotational damping force of TENGs, the C_e, C_m and C_t can be expressed as

$$\begin{cases} C_e = NBIL = B\frac{E(t)}{R_C}L = N^2B^2\frac{\int_{point1}^{point2}\dot{\theta} l dl}{R_c}\int_{point1}^{point2} dl \\ C_m = 2mc_m\sqrt{\frac{g}{R}}R\dot{\theta} \\ C_t = \frac{y(x)Ebh_T^3}{2x^2(x-3a)}c \end{cases} \tag{7}$$

where B is the magnetic field density; L is the effective length of the coils when magnetic induction line cutting the coils; R_c is the impedance of the coils; and c_m is the mechanical damping coefficient; c is the frictional coefficient; h_T is the thickness of the TENG blade (FEP//Cu//FEP).

To maximize the output power of the EMG, the output performances of the device with different combination of magnets were systematically investigated. Fig. 2g illustrated the output voltage and the output density (V_{OC} divided by the total weight of the device) of the EMG against different combination of magnets at a constant frequency of 2 Hz and amplitude of 8 cm. It is found that the V_{OC} is closely related to the number and diameter of the magnets and reaches the maximum value when 6 magnets with diameter of 25 mm are stacked together. However, as can be seen from the chart, the voltage density reaches the maximum value when 4 magnets of ∅20 mm are stacked and starts to decrease as the number of magnets increases. Therefore, the EMG configuration with 4 magnets in diameter of 20 mm is adopted in the following test.

2.3. Structure optimization and output characteristics

A series of experiments were carried out to optimize the output performance of the device with different configurations, such as different thickness of the Cu and FEP, and different length of the blade. The linear motor which is controlled through a function generator with adjustable frequency and amplitude was used to provide the external sinusoidal excitation with a frequency of 2 Hz and amplitude of 10 cm as shown in Fig. S3.

Firstly, the effect of the thickness of Cu electrode on the output performance of the EMG and TENG was investigated systematically. In this experiment, the FEP thin film with the thickness of 0.05 mm was sandwiched by the double sides of copper electrode of different thickness from 0.01 mm to 0.1 mm. It can be noted from Fig. 3a and b that the root mean square (RMS) voltage density (output voltage divided by the area rotation and the area of TENG) of the EMG increases with the decrease of the Cu electrode thickness. Meanwhile, the RMS voltage density of the TENG reaches the maximum value when the thickness of the Cu electrode is 0.05 mm. According to Eq. (3), the increase of the Cu electrode thickness results in the increase of the spring constant, which leads to the increase of the elastic force. As a consequence, the increasing elastic force has significant effect on the rotation of the rotor magnets. Considering that the energy harvesting of the EMG is higher than that of the TENG, therefore, in the following experiment, the thickness of the Cu electrode is adopted as 0.01 mm. Three types of FEP blades with different thickness of 0.01, 0.05 and 0.1 mm are considered. Fig. 3c and d illustrate the Voc and the RMS voltages density of the EMG and TENG with different thickness of the FEP film, indicating that the output performances of the EMG remains basically the same of 17.5 V as the thickness of the FEP changes. The V_{OC} of the TENG is closely related to the thickness of FEP. The RMS voltage density increases from 4 V/cm^2 to the maximum value of 6 V/cm^2 at the thickness of 0.1 mm. According to Eqs. (3) and (4), the increase of the FEP thickness results in the increase of the spring constant and decrease of the deflection of the blade, which introduces more contact area between the Cu electrode and the FEP film. Therefore, the V_{OC} of the TENG will increase with the thicker FEP film. Also, the deformation photograph of the TENG with different thickness of FEP after 30 min of testing (4 Hz, 10 cm) can be seen in Fig. S4 in supporting information. As can be seen from Fig. S4, when the thickness of FEP is 0.01 and 0.05 mm, the deformation of the TENG blade is severe, and when the thickness of FEP is 0.1 mm, the TENG blade is substantially free of deformation. So, the thickness of the FEP is determined as 0.1 mm. The length of the blade is also a major factor that affect the electric output of the TENG. As depicted in Fig. 3e and f, the V_{OC} of the EMG does not change much with changing the length of the blade, while the V_{OC} and RMS voltage density of the TENG reaches the maximum when the length of the blade is about 20 mm. As a result, the blade with a length of 20 mm is used in the following experiments.

Secondly, the influence of the frequency and amplitude on the output performance of the EMG and TENG was studied, and the results are shown in Fig. 4. When the frequency of the excitation force is varied from 1 Hz to 4 Hz with the amplitude maintaining a constant value of 10 cm, the output peak-to-peak voltage of the EMG increases from 2.6 to 13 V. The output peak-to-peak voltage of the TENG correspondingly goes from 0 to 180 V, as shown in Fig. 4a and b. While the amplitude of the excitation force changes from 2 cm to 14 cm with the frequency remaining constant of 2 Hz, the output peak-to-peak voltage of the EMG increases from 1.5 to 9.6 V, and the output of the TENG also goes from 1 to 230 V, as shown in Fig. 4c and d. Based on Eq. (4), when the excitation frequency and amplitude are large, the pendulum rotor magnets will obtain a greater angular velocity. At the same time, the concentrated load F_T will be larger, which leads to a large output voltage of the TENG. It is verified that in a certain frequency and amplitude range, when the amplitude is constant, the output performance increases with the increase of the frequency. However, when the frequency is constant, the larger the amplitude, the better the output performance.

Additionally, the number of blades of the RPHG configuration was investigated. As depicted in Fig. 4e, the output of the EMG is not significantly affected by fixing 1 or 2 TENG blades, and the RMS voltage density is about 0.053 V/cm^2. When the number of the TENG blades are increased to 3–4, the output RMS voltage density is obviously reduced. The increasement of more TENG blades will seriously affect the rotation of the pendulum rotor. As a result, the output RMS voltage density at first increases with the number of the TENG blades and reaches the maximum value of 9.56 V/cm^2 when there are 3 TENG blades, and then decreases sharply to 6.7 V/cm^2 when the blade number increases to 4. The main reason is that the dense arrangement of TENG blades limit the motion of the rotor magnets, the converted kinetic energy is dissipated by friction. Hence, the optimal configuration of the TENG blades are defined as 2 blades positioned in the middle, where the output performance of the EMG is not affected too much, while the output of the TENG has a relatively large. Additionally, The peak-to-peak short-circuit current of the EMG part can reach to 50 mA, and the peak-to-peak short-circuit current of the TENG part is about 7 μA under the external sinusoidal excitation with frequency of 2 Hz and amplitude of 14 cm (see Fig. S6 in supporting information).

The instantaneous peak output power of the RPHG was measured under the external excitation with frequency of 2 Hz and amplitude of 10 cm. Usually, the effective output power of the RPHG depends on the matched load resistance. Once a variable external load is connected to the EMG and TENG, the output voltage rises as the load resistance increases, as displayed in Fig. 5a and b. The output power is equivalent to the Joule heating of the load resistor, which can be calculated as U^2/R, where U is open-circuit voltage and R is the load resistance. As shown in Fig. 5a, the instantaneous peak output power of the EMG increases from 75 mW to 265 mW as the resistance changes from 10Ω to 75Ω and then

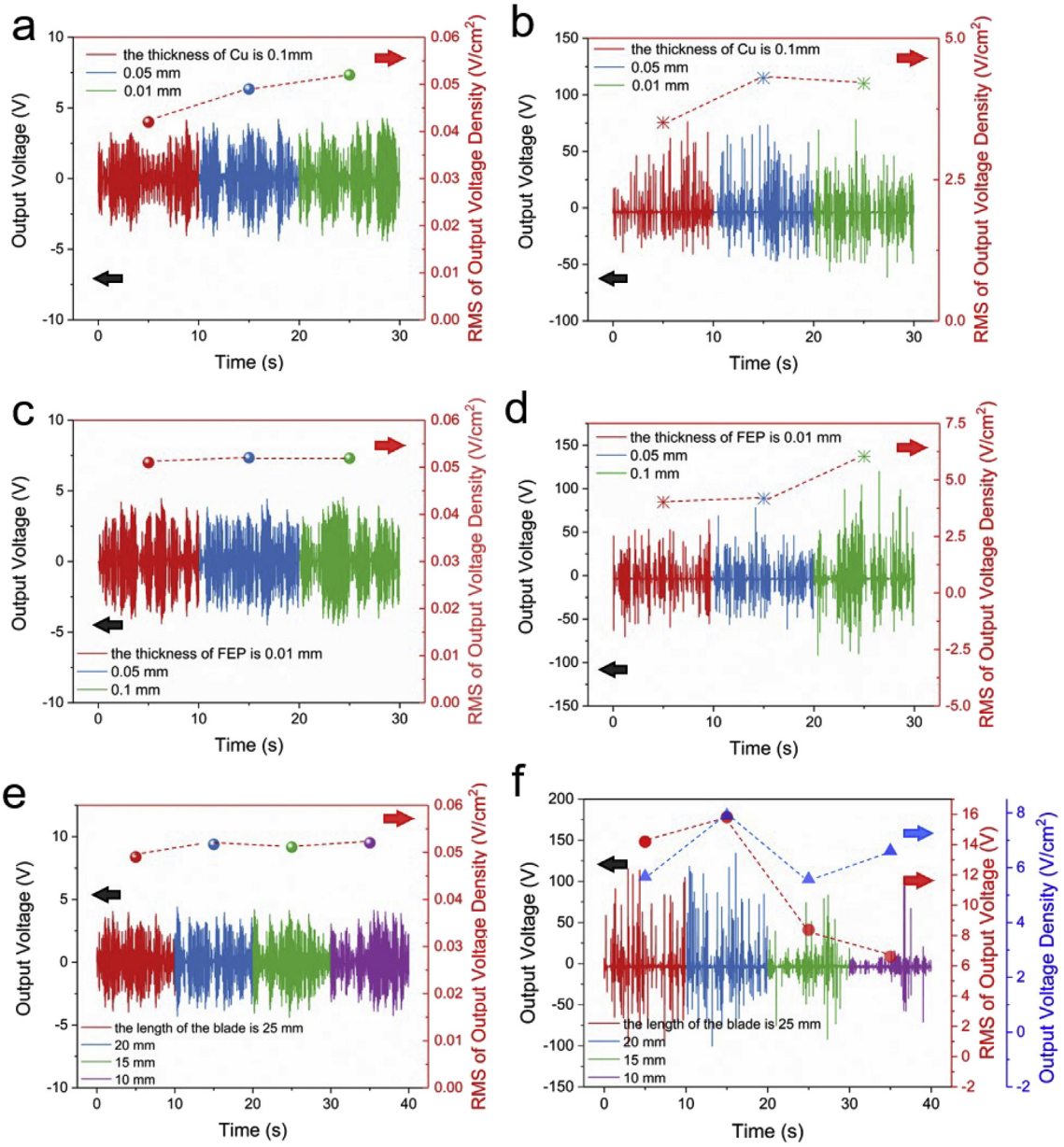

Fig. 3. Output voltage of the fabricated device with different blade configuration tested on the linear motor. (a, b) Open-circuit voltage and root mean square (RMS) of the output voltage density generated by the EMG and TENG with different thickness of Cu electrode of the blade at a constant frequency of 2 Hz and amplitude of 10 cm. (c, d) Open-circuit voltage and RMS voltage density generated by the EMG and TENG with different thickness of FEP of the blade at a constant frequency of 2 Hz and amplitude of 10 cm. (e, f) Open-circuit voltage, RMS voltage and RMS voltage density generated by the EMG and TENG with different length of blade at a constant frequency of 2 Hz and amplitude of 10 cm.

decreases with the larger load resistance, indicating a maximum power density of 79.9 W/m^2. Meanwhile, there is a similar trend for the TENG. As shown in Fig. 5b the maximal instantaneous peak power of the TENG is 0.65 mW under a matched load resistance of 10 MΩ which gives the power density of 3.25 W/m^2 under the contact area of about 2 cm^2. Furthermore, the charging capability of the RPHG is characterized by using a 22 μF capacitor. The external excitation of the frequency is 2 Hz and the amplitude is 10 cm in this experiment. The corresponding circuit diagram is illustrated in Fig. 5c and the voltage of the capacitor against time is shown in Fig. 5d. The TENG has a larger charged voltage than that of the EMG, although the EMG has a faster charging speed than that of the TENG. This means that over a certain period, the capacitance voltage charged by the TENG will be larger than that charged by the EMG. The charging voltage of the capacitor by the EMG and TENG reaches 3 V and 6.2 V after 45s, separately. Although the EMG has a larger output power, which can charge the capacitor quickly to 3 V, its charging level is limited by low output voltage. Due to the higher output voltage and lower output power of the TENG, the capacitor can be charged to a high voltage over a long time. By connecting the two modules in parallel, the hybrid charging has the characteristics of fast charging speed and high charging level, as shown in Fig. 5d. While the hybridized EMG and TENG, has a much better charging performance than the individual EMG or TENG, which benefit from the hybridization configuration. Additionally, the RPHG can be also utilized as a power source for powering some electronics without using a storage unit. As illustrated in Fig. 5e and f, 14 blue LEDs are connected in series and lighted by the TENG. Meanwhile, about 400 blue LEDs are connected in parallel and lighted by the EMG. Also, the frequency and amplitude of the external excitation are 2 Hz and 10 cm respectively.

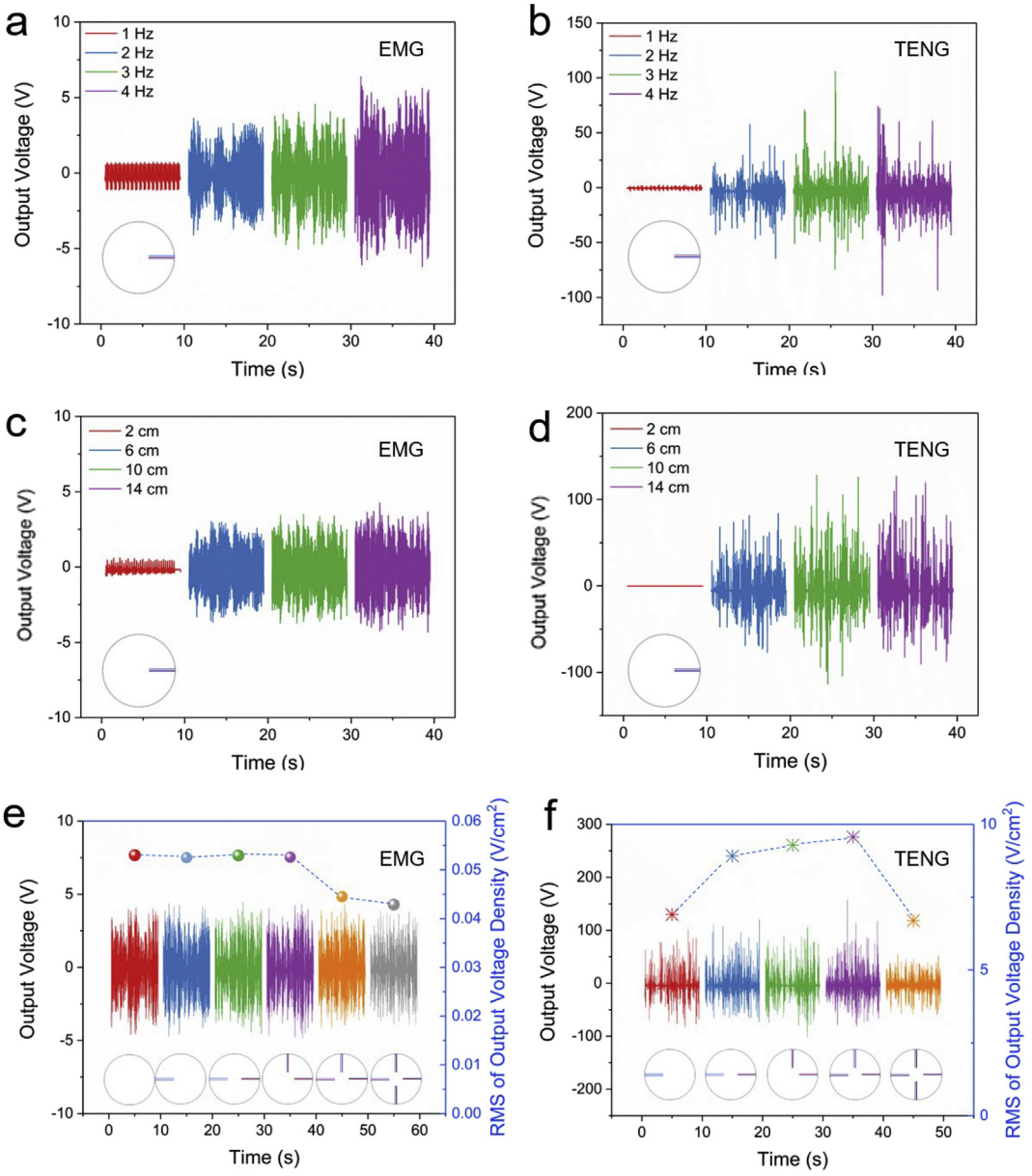

Fig. 4. (a, b) The output voltage of the EMG and TENG for a varied frequency from 1 Hz to 4 Hz with a constant amplitude of 10 cm. (c, d) The output voltage of the EMG and TENG for a varied amplitude from 2 cm to 14 cm with a constant frequency of 2 Hz. (e, f) The output voltage and RMS voltage density of EMG and TENG in different number of TENG blades configuration combinations.

2.4. Extract energy from body motions and water waves

On the basis of the above-mentioned characteristics, the output performance of the optimized RPHG with the inset configuration were investigated systematically. To harvest the irregular and low-frequency biomechanical energy, we mounted the RPHG at different locations of one tester. As shown in Fig. 6a, the RPHG is held in the tester's hand and tested on a treadmill at different speed (2–8 km/h). As shown in Fig. 6b and c, both the EMG and TENG modules perform quite well and the output voltages increase as the speed increases. When the speed reaches to 8 km/h, the instantaneous peak-to-peak output voltage of the EMG and TENG is 9.5 V and 150 V, respectively. In the demonstration, 60 red LEDs were mounted on the arm and connected with the RPHG to show its direct application on driving electronic devices. In Fig. 6a and Movie S1 and S2 in the supplementary information, the generator has sufficient power to drive dozens of red LEDs by harvesting the biomechanical energy. Then the RPHG was mounted on the tester's waist to extract kinetic energy from rope skipping, as shown in Movie S3 of the supplementary information. A data acquisition card was used to collect the test data for real time monitoring. The output voltage of the EMG and TENG for different skipping speed is depicted in Fig. 6e and f. The higher and denser output voltage was obtained at higher skipping speed. The aforementioned human body tests demonstrate that the proposed RPHG can generate considerable electricity from various human activities. From a practical point of view, the RPHGs can be employed with energy storage devices to act as backup emergency power sources for commercial electronic sensors or wearable electronics, especially in some special scenario such as jungles and snow mountains.

Supplementary video related to this article can be found at https://doi.org/10.1016/j.nanoen.2019.103871.

The RPHG also shows a wide range of application prospects in ocean wave energy harvesting. Considering the influence of humidity on the output performance of the TENGs, we have done humidity test and the

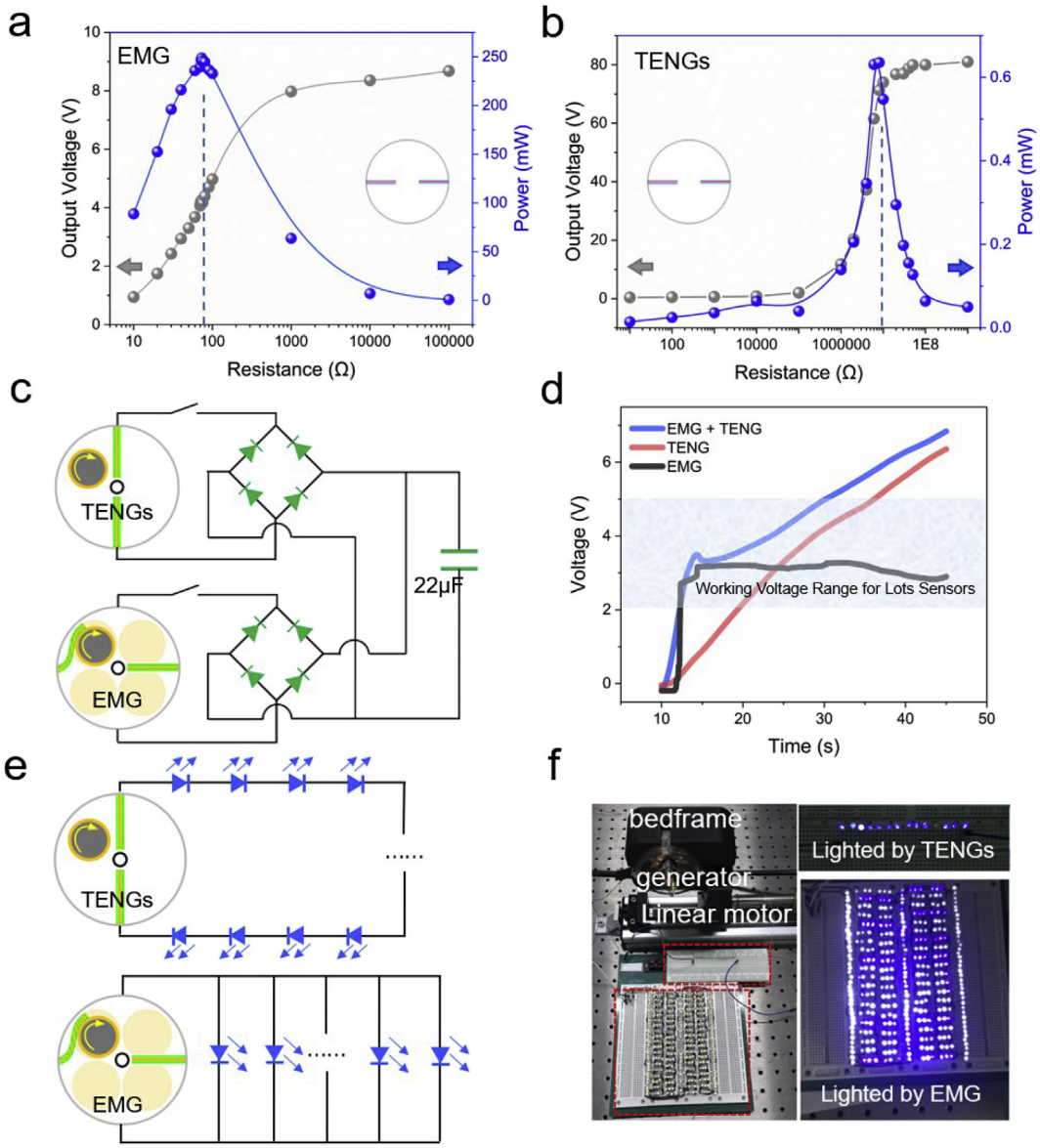

Fig. 5. Output performance of the hybrid generator under the frequency of 2 Hz and amplitude of 10 cm. (a, b) Output voltage and power of the EMG and TENG. (c) The corresponding circuit diagram of charging experiment. (d) Charging curve of the EMG, TENG, and the hybrid generator when the capacitor is 22 μF. (e) Schematic diagram of the connection between the TENG and 14 blue LEDs, the EMG and about 400 blue LEDs.

relationship between the output voltage of the TENG and the humidity is depicted in Fig. S5b in Supporting Information under the excitation of 1.5 Hz and 10 cm amplitude. When the humidity is above 50%, the output voltage of TENG drops very little. As the humidity continues to increase, the output voltage of TENG drops significantly. When the humidity increases to 90%, the output voltage of TENG drops by 80%. To eliminate the humidity effect, as shown in Fig. S7, the scheme of the RPHG for ocean wave harvesting is totally inside the sealed buoy. So, we assumed the influence of humidity on the output performance of the device can be ignored. As shown in Fig. 7a, our device is placed vertically in a sealed box, floating on the water surface. The pendulum rotor magnets perform a sway motion similar to the motion of the waves, and occasionally scrape through the TENG, the relationship between the output voltage of the EMG and TENG and the height of waves is depicted in Fig. 7b and c. It can be seen that as the wave height increases, the output voltage of the EMG increases continuously. When the wave height is 10 cm, the peak-to-peak output voltage can reach 3.4 V. Meanwhile, when the wave height is less than 8 cm, there is no output of TENG due to the lack of kinetic energy to excite the pendulum rotor to scrape through the TENG. As the wave height reaches 10 cm, the swing amplitude of the pendulum rotor increases significantly. The peak-to-peak output voltage of the TENG is 80 V, which is much larger than that of 8 cm. To illustrate the output of the RPHG in water waves, driven by artificial waves in the sealed box, the RPHG placed horizontally on the buoy can light up dozens of red LEDs as shown in Movie S4 in supplementary information.

Supplementary video related to this article can be found at https://doi.org/10.1016/j.nanoen.2019.103871.

Additionally, we made a simple buoy to implant the device and put it into the Tai Lake for testing as shown in Fig. 7d, Movie S5 in supplementary information. The RPHG can be placed vertically and horizontally (see Figs. S7 and S8 in supporting information). The water waves are irregular and complicated, with the frequency of less than 2 Hz along random directions. Fig. 7e and f shows the voltage waveforms of the RPHG excited by lake water waves of about 20 cm high and a frequency of 1 Hz. When it was placed vertically in the buoy, the peak-to-peak output voltage of EMG and TENG can reach 3.4 V and 80 V, respectively, as shown in Fig. 7e and f. However, the output signal

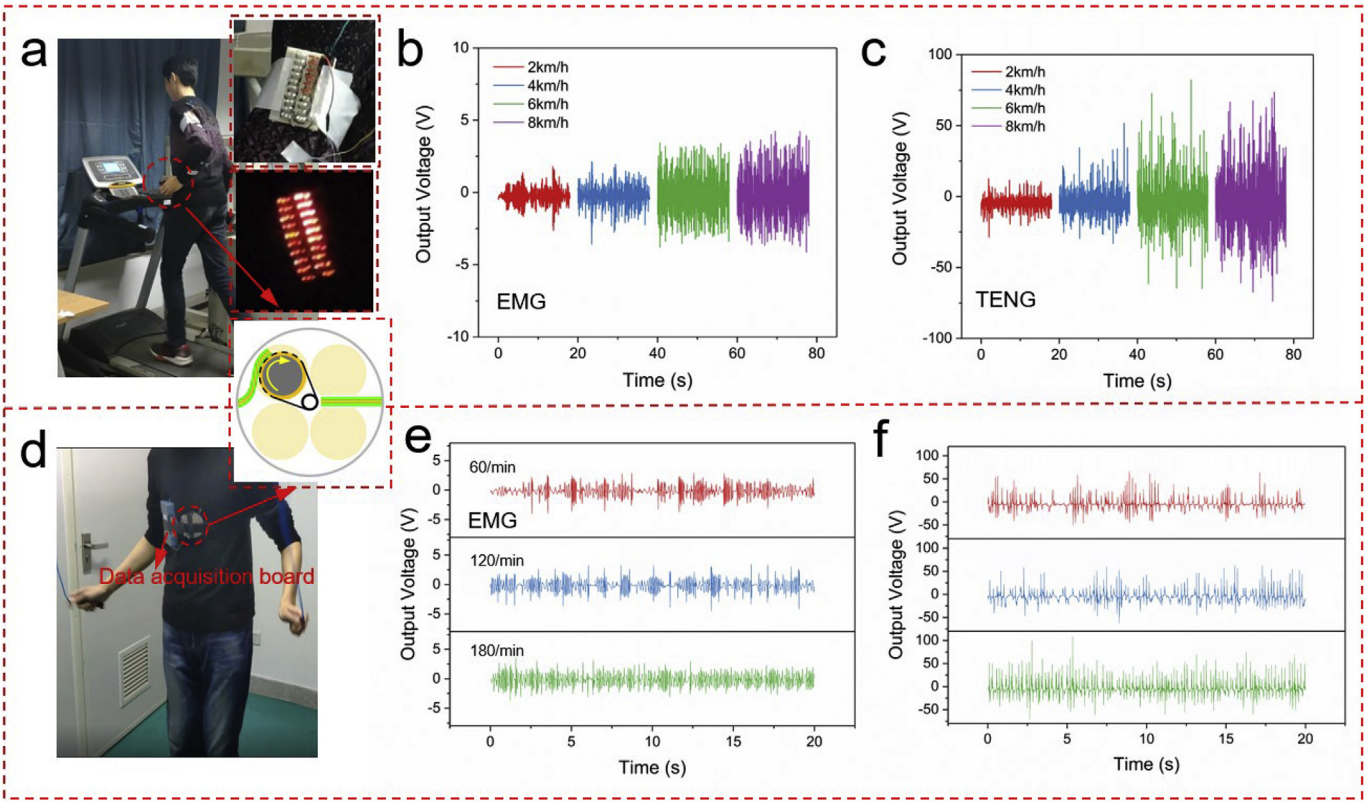

Fig. 6. Demonstration of the hybrid generator for energy scavenging in human motion. (a) One tester with the hybrid generator in his left hand running a test on a treadmill at different speed. (b) Dependence of output voltage of the EMG on the speed. (c) Dependence of output voltage of the TENGs on the speed. (d) The hybrid generator collects the kinetic energy when human rope skipping. (e, f) Dependence of output voltage of the EMG and TENGs on the different skipping times in 1 min.

of the TENG has obvious discontinuity, where the pendulum rotor swing to a small extent and cannot trigger the TENG continuously. Because the turbulent waves cause the buoy to rotate, which prevents the vertical RPHG from being effectively excited by the waves. But the direction of the wave near the shore is relatively simple, so there is no significant impact on the output of the RPHG. Fig. 7g and h shows the effectiveness of the RPHG placed horizontally in the buoy under the same wave condition, where the pendulum rotor would rotate under the excitation in any directions. The results indicate that the EMG peak-to-peak voltage of the RPHG is lower when it is placed horizontally than that when vertically, which is about 3.2 V and 3.4 V, respectively. The TENG's peak-to-peak voltages were the relatively close, at 60 V. However, the continuity of the output signals is very poor when the RPHG placed vertically. According to the characteristics of different sea areas, this provides a basis for the optimal placement of the RPHG. The RPHG can be placed vertically near the shoreline where the wave direction is relatively uniform, while it should be placed horizontally in the deep sea where the wave direction often changes.

Supplementary video related to this article can be found at https://doi.org/10.1016/j.nanoen.2019.103871.

3. Conclusion

In summary, to efficiently harvest mechanical energy from human motion and blue energy, a rotational pendulum electromagnetic-triboelectric hybridized generator based on pendulum rotor magnets is proposed. With the rotation of the rotor magnets, the EMG module will produce the electromagnetic induced electricity, and the copper around rotor magnets will periodically get in contact with the flexible blades and slide through FEP layers on blades to generate the triboelectric induced output as the TENG module. To optimize the electrical-output performance of the device, measurements were carried out for a certain external excitation of linear motor with different configurations (thickness of Cu and FEP, length of the blade). Additionally, the output performance of the RPHG was systemically investigated by same frequency and amplitude under different configuration of number and position of the blades. After the optimization of the configuration of the hybrid generator, the maximum power density of 3.25 W/m^2 and 79.9 W/m^2 are obtained at a driving frequency of 2 Hz and amplitude of 14 cm by the TENG and EMG, respectively. A much better charging performance than the individual EMG or TENG can be observed on the RPHG. Also, the RPHG under the external excitation can light up hundreds of LEDs. Several practical tests were conducted to verify the effectiveness of the RPHG, such as harvesting the kinetic energy from human motion and lake waves. When the speed is 8 km/h, the instantaneous peak-to-peak output voltage of the EMG and TENG is 9.5 V and 150 V, respectively. When the wave is 20 cm high and the frequency is about 1 Hz, the voltage peak-to-peak values of EMG and TENG can reach 3.4 V and 80 V, respectively. It can be seen that the output performance of the device in ultra-low-frequency and irregular vibration is considerable. Through increasing the number of the coils, choosing a much stronger magnetic with larger size, enlarging the surface of the friction layer, etc., the performance of the RPHG can be further improved. This fabricated device shows a great potential for realizing the long-term power supply of the wearable IoT and blue energy applications.

4. Methods

4.1. Fabrication of the RPHG

The harvester is fabricated through machining and 3D-printing technology. The harvester is mainly acrylic, which has a total dimension of Φ71mm in diameter and 40 mm in height, including a pendulum

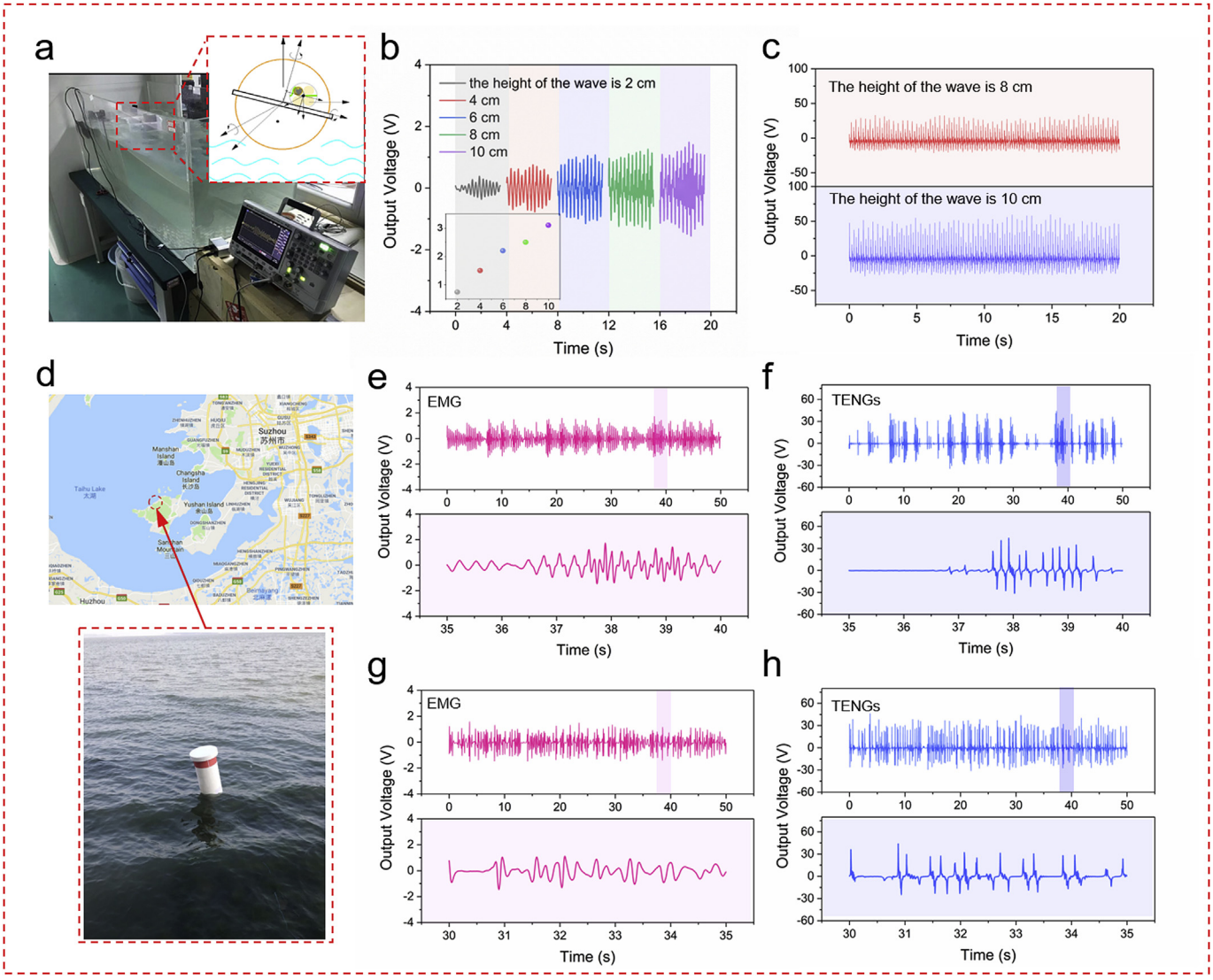

Fig. 7. Demonstration of the hybrid generator for energy scavenging in water waves. (a) Photographs of the hybrid generator driven by the water wave system equipped with two variable pumps. (b, c) Dependence of output voltage of the EMG and TENG on the height of the waves. (d) Photographs of the hybrid generator tested in lake. (e, f) The output voltage of the EMG and TENG when placed vertically. (g, h) The output voltage of the EMG and TENG when placed horizontally.

rotor, coils, TENG blades and a cylindrical frame. The pendulum rotor is composed of an aluminum alloy support, four disk-shaped magnets and a copper ring curling around the magnets, while the pendulum rotor is assembled on the center shaft by two ceramic bearings. The pendulum rotor magnets are made of NdFeB, and four coils are copper wire.

The TENG blade has a multiple-layer architecture, including a flexible substrate sandwiched by one copper films and two fluorinated ethylene propylene (FEP) films symmetrically. One side of the TENG blade was fixed on an acrylic sheet around the frame, while the other side is freestanding. The fluorinated ethylene propylene was bought online.

4.2. Measurement system

The hybrid generator is anchored on the linear motor (PF02-37*100) to test the output performance of the device under different excitations. The output current of the device was measured by a low-noise current preamplifier (Stanford Research SR570). The output voltage signals of the RPHG excited by linear motor and water waves were recorded and displayed through two digital oscilloscopes (Agilent DSO-X2014A, HOS-MS6100). The output voltage signals of the RPHG excited by rope skipping were recorded by data acquisition board (MC BTH-1208LS).

A wave simulation system equipped with two variable flow pumps was applied to simulate the motion of water waves in an actual environment and provide a stable external force to make the rotor magnets rotate.

Author contributions

The work presented in this paper was a collaboration of all authors. Cheng Hou and Tao Chen designed the RPHG and wrote the main manuscript text. Cheng Hou and Yunfei Li fabricated the RPHG and characterized the device's performance. Cheng Hou and Qiongfeng Shi analysed the data. Huicong Liu, Lining Sun and Chengkuo Lee contributed funds and manuscript modification. All authors discussed and commented on the manuscript.

Acknowledgements

This work is funded by the National Science Foundation of China (Grant No. 41527901 and No. 51875377); Qingdao National

Laboratory for Marine Science and Technology (Grant No. 2017ASKJ01); Qing Lan Project; HIFES Seed Funding-2017-01 grant (R-263-501-012-133) “Hybrid Integration of Flexible Power Source and Pressure Sensors” at the National University of Singapore. Singapore-Poland Joint Grant (R-263-000-C91-305) “Chip-Scale MEMS Micro-Spectrometer for Monitoring Harsh Industrial Gases” by Agency for Science, Technology and Research (A*STAR), Singapore.

Appendix A. Supplementary data

Supplementary data to this article can be found online at https://doi.org/10.1016/j.nanoen.2019.103871.

References

[1] J. Nie, M. Ji, Y. Chu, X. Meng, J. Zhong, Y. Wang, L. Lin, Nano Energy 58 (2019) 528–535.
[2] K. Tao, L. Tang, J. Wu, S.W. Lye, H.L. Chang, J.M. Miao, J. Microelectromech. Syst. 27 (2018) 276–288.
[3] P. Wang, H.J. Du, Rev. Sci. Instrum. 86 (2015) 1131–1134.
[4] M. Halim, R. Rantz, Q. Zhang, L. Gu, K. Yang, S. Roundy, Appl. Energy 217 (2018) 66–74.
[5] P. Wang, K. Tanaka, S. Sugiyama, X. Dai, X. Zhao, J. Liu, Microsyst. Technol. 15 (2009) 941–945.
[6] H. Liu, B.W. Soon, N. Wang, C.J. Tay, C.G. Quan, C. Lee, J. Micromech. Microeng. 22 (2012) 125020.
[7] H. Liu, K.H. Koh, C. Lee, Appl. Phys. Lett. 104 (2014) 053901.
[8] H. Liu, Y. Qian, N. Wang, C. Lee, J. Microelectromech. Syst. 23 (2014) 740–749.
[9] H. Liu, C. Hou, J. Lin, Y. Li, Q. Shi, T. Chen, L. Sun, C. Lee, Appl. Phys. Lett. 113 (2018) 203901.
[10] Y. Yang, L. Tang, J. Intell. Mater. Syst. Struct. 20 (2009) 2223–2235.
[11] M. Kim, M. Hoegen, J. Dugundji, B.L. Wardle, Smart Mater. Struct. 19 (2010) 045023.
[12] L. Zhang, J. Lu, R. Takei, N. Makimoto, T. Itoh, T. Kobayashi, Rev. Sci. Instrum. 87 (2016) 085005.
[13] H. Liu, Y. Qian, N. Wang, C. Lee, J. Microelectromech. Syst. 23 (2014) 740–749.
[14] C.T. Pan, T. Wu, J. Micromech. Microeng. 17 (2007) 120.
[15] B. Yang, C. Lee, R.K. Kotlanka, J. Xie, S.P. Lim, J. Micromech. Microeng. 20 (2010) 065017.
[16] P. Cheng, Y. Liu, Z. Wen, H. Shao, A. Wei, X. Xie, C. Chen, Y. Yang, M. Peng, Q. Zhuo, X. Sun, Nano Energy 54 (2018) 156–162.
[17] M. Zhu, Q. Shi, T. He, Z. Yi, Y. Ma, B. Yang, T. Chen, C. Lee, ACS Nano 13 (2019) 1940–1952.
[18] T. He, Z. Sun, Q. Shi, M. Zhu, D.V. Anaya, M. Xu, T. Chen, M.R. Yuce, A.V. Thean, C. Lee, Nano Energy 58 (2019) 641–651.
[19] H. Liu, J. Zhong, C. Lee, S.W. Lee, L. Lin, Appl. Phys. Rev. 5 (2018) 041306.
[20] T. Chen, Q. Shi, M. Zhu, T. He, L. Sun, L. Yang, C. Lee, ACS Nano 12 (2018) 11561–11571.
[21] T. Chen, M. Zhao, Q. Shi, Z. Yang, H. Liu, L. Sun, J. Ouyang, C. Lee, Nano Energy 51 (2018) 162–172.
[22] G. Liu, J. Chen, H. Guo, M. Lai, X. Pu, X. Wang, C. Hu, Nano Res. 11 (2018) 633–641.
[23] Y. Yang, H. Zhang, Z.H. Lin, Y.S. Zhou, Q. Jing, Y. Su, J. Yang, J. Chen, C. Hu, Z.L. Wang, ACS Nano 7 (2013) 9213–9222.
[24] G. Liu, J. Chen, Q. Tang, L. Feng, H. Yang, J. Li, Y. Xi, X. Wang, C. Hu, Adv. Energy Mater. 8 (2018) 1703086.
[25] J. Chen, X. Pu, H. Guo, Q. Tang, L. Feng, X. Wang, C. Hu, Nano Energy 43 (2018) 253–258.
[26] X. Pu, H. Guo, Q. Tang, J. Chen, L. Feng, G. Liu, X. Wang, Y. Xi, C. Hu, Z.L. Wang, Nano Energy 54 (2018) 453–460.
[27] R. Lei, H. Zhai, J. Nie, W. Zhong, Y. Bai, X. Liang, L. Xu, T. Jiang, X. Chen, Z.L. Wang, Adv. Mater. 4 (2019) 1800514.
[28] L. Xu, T. Jiang, P. Lin, J.J. Shao, C. He, W. Zhong, X. Chen, Z.L. Wang, ACS Nano 12 (2018) 1849–1858.
[29] M. Xu, T. Zhao, C. Wang, S.L. Zhang, Z. Li, X. Pan, Z.L. Wang, ACS Nano 13 (2019) 1932–1939.
[30] X. Liang, T. Jiang, G. Liu, T. Xiao, L. Xu, W. Li, F. Xi, C. Zhang, Z.L. Wang, Adv. Funct. Mater. (2019) 1807241.
[31] U. Khan, S.W. Kim, Triboelectric nanogenerators for blue energy harvesting, ACS Nano 10 (2016) 6429–6432.
[32] C.R.S. Rodrigues, C.A.S. Alves, J. Puga, A.M. Pereira, J.O. Ventura, Nano Energy 30 (2016) 379–386.
[33] M.T. Rahman, M. Salauddin, P. Maharjan, M.S. Rasel, H. Cho, J.Y. Park, Nano Energy 57 (2019) 256–268.
[34] P. Wang, L. Pan, J. Wang, M. Xu, G. Dai, H. Zou, K. Dong, Z.L. Wang, ACS Nano 12 (2018) 9433–9440.
[35] S. Lee, S.H. Bae, L. Lin, Y. Yang, C. Park, S.W. Kim, S.N. Cha, H. Kim, Y.J. Park, Z.L. Wang, Adv. Funct. Mater. 23 (2013) 2445–2449.
[36] S. Wang, X. Mu, Y. Yang, C. Sun, A.Y. Gu, Z.L. Wang, Adv. Mater. 27 (2015) 240–248.
[37] X. Wang, S. Niu, F. Yi, Y. Yin, C. Hao, K. Dai, Y. Zhang, Z. You, Z.L. Wang, ACS Nano 11 (2017) 1728–1735.
[38] Z.L. Wang, J. Chen, L. Lin, Energy Environ. Sci. 8 (2015) 2250–2282.
[39] Y. Zi, S. Niu, J. Wang, Z. Wen, W. Tang, Z.L. Wang, Nat. Commun. 6 (2015) 8376.
[40] R.K. Gupta, Q. Shi, L. Dhakar, T. Wang, C.H. Heng, C. Lee, Sci. Rep. 7 (2017) 41396.
[41] Z. Li, J. Chen, J. Zhou, L. Zheng, K.C. Pradel, X. Fan, H. Guo, Z. Wen, M.H. Yeh, C. Yu, Z.L. Wang, Nano Energy 22 (2016) 548–557.
[42] J. Chen, J. Yang, H. Guo, Z. Li, L. Zheng, Y. Su, Z. Wen, X. Fan, Z.L. Wang, ACS Nano 9 (2015) 12334–12343.
[43] C. Wu, X. Wang, L. Lin, H. Guo, Z.L. Wang, ACS Nano 10 (2016) 4652–4659.
[44] H. Askari, E. Asadi, Z. Saadatnia, A. Khajepour, M.B. Khamesee, J. Zu, Nano Energy 32 (2017) 105–116.
[45] P. Wang, R. Liu, W. Ding, P. Zhang, L. Pan, G. Dai, H. Zou, K. Dong, C. Xu, Z.L. Wang, Adv. Funct. Mater. 28 (2018) 1705808.
[46] C. Zhang, W. Tang, C.B. Han, F.R. Fan, Z.L. Wang, Adv. Mater. 26 (2014) 3580–3591.
[47] H. Guo, Z. Wen, Y. Zi, M.H. Yeh, J. Wang, L. Zhu, C. Hu, Z.L. Wang, Adv. Energy Mater. 6 (2016) 1501593.
[48] Z. Wen, H. Guo, Y. Zi, M.H. Yeh, X. Wang, J. Deng, J. Wang, S. Li, C. Hu, L. Zhu, Z.L. Wang, ACS Nano 10 (2016) 6526–6534.
[49] G. Zhu, J. Chen, T. Zhang, Q. Jing, Z.L. Wang, Nat. Commun. 5 (2014) 3426.
[50] X. Zhong, Y. Yang, X. Wang, Z.L. Wang, Nano Energy 13 (2015) 771–780.
[51] Y. Xie, S. Wang, S. Niu, L. Lin, Q. Jing, Y. Su, Z. Wu, Z.L. Wang, Nano Energy 6 (2014) 129–136.
[52] H. Zhang, Y. Yang, X. Zhong, Y. Su, Y. Zhou, C. Hu, Z.L. Wang, ACS Nano 8 (2014) 680–689.
[53] W. Tang, C. Zhang, C. Han, Z.L. Wang, Adv. Funct. Mater. 24 (2014) 6684–6690.
[54] P. Bai, G. Zhu, Y. Liu, J. Chen, Q. Jing, W. Yang, J. Ma, G. Zhang, Z.L. Wang, Cylindrical rotating triboelectric nanogenerator, ACS Nano 7 (2013) 6361–6366.
[55] M. Salauddin, R.M. Toyabur, P. Maharjan, J.Y. Park, Nano Energy 45 (2018) 236–246.
[56] X. Chen, H. Guo, H. Wu, H. Chen, Y. Song, Z. Su, H. Zhang, Nano Energy 49 (2018) 51–58.
[57] Y. Wu, X. Wang, Y. Yang, Z.L. Wang, Nano Energy 11 (2015) 162–170.
[58] K. Zhang, Y. Wang, Y. Yang, Adv. Funct. Mater. (2018) 1806435.
[59] Y. Zhu, A. Yu, R. Cao, R. Wen, M. Jia, Y. Lei, Y. Zhang, Y. Liu, J. Zhai, Adv. Electron. Mater. 4 (2018) 1800161.
[60] G.T.A. Kovacs, Micromachined Transducers Sourcebook, Simplified Chinese ed., McGraw-Hill, New York, 1998, pp. 135–136.

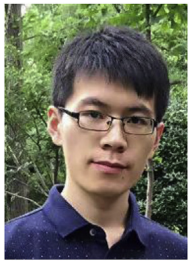

Cheng Hou is currently a Ph.D candidate majoring in Intelligent Robot in Robotics and Microsystems Center, School of Mechanical and Electrical Engineering, Soochow University since 2018. His main research interests include vibration-based MEMS/NEMS energy harvesters, practical applications in self-powered sensing, blue energy harvesting and self-powered MEMS/NEMS system for IoTs and MEMS devices for robotic and medical applications.

Tao Chen received the B.Sc. degree in Mechanica l Design, Manufacturing and Automation, M.Sc. degree in Mechatronic Engineering, and Ph.D. degree in Mechatronic Engineering from Harbin Institute of Technology, Harbin, China, in 2004, 2006, and 2010, respectively. He is a visiting scholar in National University of Singapore in 2018. He is currently an associate professor at Soochow University, Suzhou, China. His main research interests include MEMS, sensors, and actuators.

Yunfei Li received the B.Eng. degree from the School of Mechanical Engineering, Zhengzhou University, Zhengzhou, China, in 2016. He is currently pursuing the M.Eng. degree in Robotics and Microsystems Center, School of Mechanical and Electrical Engineering, Soochow University. His research interests include practical applications in self-powered sensing and blue energy harvesting.

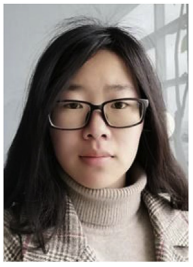

Manjuan Huang received the B.Eng. degree in mechatronics engineering from Soochow University, Suzhou, China, in 2017. She is currently pursuing the M.Eng. degree in Robotics and Microsystems Center, School of Mechanical and Electrical Engineering, Soochow University. Her research interests include MEMS-based piezoelectric vibration energy harvester.

Qiongfeng Shi received his B.Eng. degree from Department of Electronic Engineering and Information Science at University of Science and Technology of China (USTC) in 2012. He is currently pursuing his Ph.D. degree in the Department of Electrical and Computer Engineering, National University of Singapore (NUS) under the NUS research scholarship. His research interests are focused on energy harvesters and self-powered sensors.

Huicong Liu received her Ph.D. degree from the Department of Mechanical Engineering, National University of Singapore (NUS) in 2013. She has been a Research Fellow in Department of Electrical and Computer Engineering, NUS from Aug. 2012 to Aug. 2013. Currently she is a Professor in Robotics and Microsystems Center, School of Mechanical & Electric Engineering, Soochow University, China. Her research interests are vibration-based MEMS/NEMS energy harvesters, self-powered MEMS/NEMS system for IoTs and flexible functional devices for robotic and medical applications.

Lining Sun is a currently a director of Robotics and Microsystems Center in Soochow University, and a President of College of Mechatronic Engineering in Soochow University. He gained China National Funds for Distinguished Young Scientists. His current research interests include micro-nano operational robot and equipment, advanced robot and control, and electromechanical integration equipment. He gained two National Science and Technology Award Grade II and three Provincial Science and Technology Prize Grade I. He has more than 300 academic papers being published and has more than 20 patents of invention being authorized.

Chengkuo Lee received his Ph.D. degree in Precision engineering from The University of Tokyo in 1996. Currently, he is the director of Center for Intelligent Sensors and MEMS, and an Associate Professor in the Department of Electrical and Computer Engineering, National University of Singapore, Singapore. In 2001, he cofounded Asia Pacific Microsystems, Inc., where he was the Vice President. From 2006 to 2009, he was a Senior Member of the Technical Staff at the Institute of Microelectronics, A-STAR, Singapore. He has contributed to more than 300 international conference papers and extended abstracts and 270 peer-reviewed international journal articles.